JOURNAL OF MATERIALS SCIENCE **40** (2005) 3091 – 3100

Determination of the atomic structure of a $\Sigma 13$ $SrTiO_3$ grain boundary

J. AYACHE,*,† C. KISIELOWSKI, R. KILAAS
National Center for Electron Microscopy, Ernest Orlando Lawrence Berkeley National Laboratory, One Cyclotron Rd., Berkeley CA 94720, USA
E-mail: ayache@csnsm.in2p3.fr

G. PASSERIEUX
CSNSM-IN2P3-CNRS Batiment 108, 91405 Orsay Campus, France

S. LARTIGUE-KORINEK
CECM-CNRS 15, rue Georges Urbain, Vitry sur Seine 94400, France

New elements of a symmetric [001] 67.4° $SrTiO_3$ near $\Sigma 13$ tilt grain boundary are identified by a quantitative analysis of lattice images, reconstructed electron exit waves, and HAADF images. The analysis reveals local, geometrical variations of structural grain boundary units that relate to the presence of defects introduced by a tilt deviation of $0.65 + 0.02$ degrees from the perfect $\Sigma 13$ geometry. Sr and TiO columns are discriminated in HAADF images while the reconstructed electron exit wave reveals all oxygen columns in addition. Both methods depict the crystal and boundary structure directly while lattice imaging with a high voltage instrument requires image simulations to link the image intensity to structure. For the first time we observe a Sr column splitting by 90 pm that supports theoretical predictions. An inhomogeneous, preferential etching at the grain boundary is attributed to local charge variations and hampers a quantitative investigation and local stoichiometry. The near $\Sigma 13$ boundary forms a dense and compact structure with chemically identical columns in close proximity. Therefore, it is different from the relaxed, bulk like configurations described in previous reports.

1. Introduction

$SrTiO_3$ crystals (STO) are suitable substrates for the fabrication of high-Tc superconducting films and devices because of a favorable dielectric constant $\varepsilon = 277$ and a good lattice match to $YBa_2Cu_3O_{7-\delta}$ [1]. Bicrystalline STO substrates are used as templates for the fabrication of Josephson junctions to investigate fundamental properties of high-Tc films [2–4] where knowledge of the grain boundary (GB) structure is essential for a control of intrinsic junction characteristics. Therefore, the atomic structure of GB's in STO was examined in great detail. High Angle Annular Dark Field (HAADF) imaging in combination with Electron Energy Loss Spectroscopy (EELS) are now more frequently used to investigate grain boundaries in STO and related materials to complement direct imaging with phase contrast microscopy [5, 6]. Specifically, a 25° Σ 85 (920), a 36° $\Sigma 5$ (310), and a 67.4° $\Sigma 13$ (320) [7–10] symmetric tilt boundary as well as a 58°[001] tilt GB [11] were examined.

Structure refinements by bond valence calculations lead to models that are both charge neutral and stoichiometric [8]. In the bulk of the material, the Sr atoms are dodecahedrally coordinated. In contrast, the Ti atoms exhibit octahedral coordination with oxygen atoms. Both static [12, 13] and first principles calculations [14] of a $\Sigma 5$ (310) GB predict a compact, dense GB structure with oxygen deficiency near the core. Sr based units are calculated to be more stable than the TiO ones [15]. If Sr columns reside in close proximity, they should be half occupied and oxygen vacancies are expected to segregate to the GB [16]. Closely spaced TiO columns would lead to an excess of Ti atoms [15] since Ti occupies all available sites. In this case, an oxygen deficiency would decrease the Ti valence [11]. All configurations lead to negatively charged GBs.

Attempts were made to describe symmetric GBs with the SU/GBD (Structural Unit/Grain Boundary Dislocations) approach [17, 18]. This GB description was extended taking into account the equivalence between the two sub-lattices centered on Sr or on TiO columns [16]. For example, the Fig. 1 shows the units S and S' that are basic units of the $\Sigma 1^*(110)$ GB, a periodic arrangement of A and A' units that defines the $\Sigma 5(310)$ GB, and the

*Author to whom all correspondence should be addressed.
† *Present address*: CSNSM-IN2P3-CNRS Batiment 108, 91405 Orsay Campus, France.

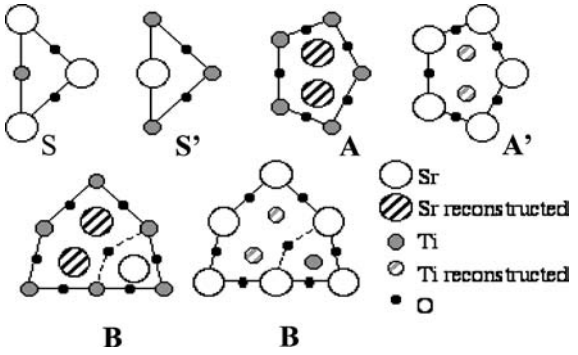

Figure 1 Structural units in $SrTiO_3$ grain boundary (courtesy of G. Dusher [16]). Units *S* and *S′* correspond to the crystal, units *B*, *B'*, *A* and *A'* correspond to the cores of primary dislocations.

units *B* or *B′* that describe the Σ5(210) GB, depending on the coincidence of Sr or TiO columns at the interface. An experimental observation of a Σ5(210) GB would be useful since its units are expected to be part of the Σ13 (320) GB if the model extension is generally applicable.

In this paper we address the structure of a Σ13 tilt GB by direct imaging with different methods: lattice imaging with a high voltage microscope, reconstruction of electron exit waves (EWR), and HAADF imaging. The approach exploits specifics of each imaging technique accessing a maximum of structural information while simultaneously highlighting the strength's and limitations of the applied methods. It will be shown that it is crucial to address each structural grain boundary unit separately since defects induce local strain—(and evidently) local charge variations that prohibit any averaging along the length of the boundary. Thereby, novel structural units are discovered and it is demonstrated for the first time that sub Ångstrom resolution can be achieved with a mid voltage instrument by imaging a non-periodic structure. A quantification of the oxygen content at the boundary is limited by sample preparation techniques that commonly create steep grooving at the interface itself.

The paper is organized in the following manner. Section 2 describes experimental details. Thereafter, results are described in detail in Section 3 that are discussed in Section 4.

2. Experimental details

The investigated Σ13 (320) tilt GB was fabricated joining two pre-oriented STO single crystals by local melting of the interface region. The deviation from the coincidence orientation was determined by LACBED. We utilized a comparison of simulations with experiments to reach a high degree of angular accuracy [19]. A tilt deviation from the ideal Σ13 geometry of $\Delta\theta = 0.65^\circ \pm 0.02^\circ$ gives rise to a misorientation angle of 68.05°.

Samples for TEM observation were prepared by tripod polishing. The thickness of the foils was a few 100 nm thereafter. Such samples are thin enough for HAADF imaging. For lattice imaging and exit wave reconstruction the foils were additionally thinned in a low voltage ion mill operated at 500 eV together with sample cooling to avoid contamination. Thereby we obtained 40–200 Å thin samples.

Classic HRTEM imaging was performed along [001] zone axis with a Jeol ARM operated at 800 KV that exhibits a Scherzer point resolution of 1.6 Å. Phase and amplitude images of the complex electron exit wave were reconstructed from 20 lattice images recorded with a CM300 FEG/UT instrument that allows for sub Ångstrom resolution because of a 0.8 Å information limit [20, 21]. HAADF images (HAADF) were recorded with a Tecnai F20 Ultra twin STEM/TEM with a smallest beam size of 1.4 Å.

The image simulations were performed by multislice calculations utilizing the McTempas and Crystal KIT software packages [22]. They were applied to interpret the HRTEM lattice image and the reconstructed electron exit wave. Simulations of the HAADF image were omitted since the large and undetermined crystal thickness limits their validity.

The considered images of the grain boundary are shown in Fig. 2. A significant contrast or pattern change at the boundary reveals that the samples are grooved, which in case of the HAADF image makes an identification of structural GB units challenging. Therefore, the HAADF image was processed for a separation of the image pattern from the rapidly varying background signal that obscures recognition of the pattern at the interface as shown in Fig. 3.

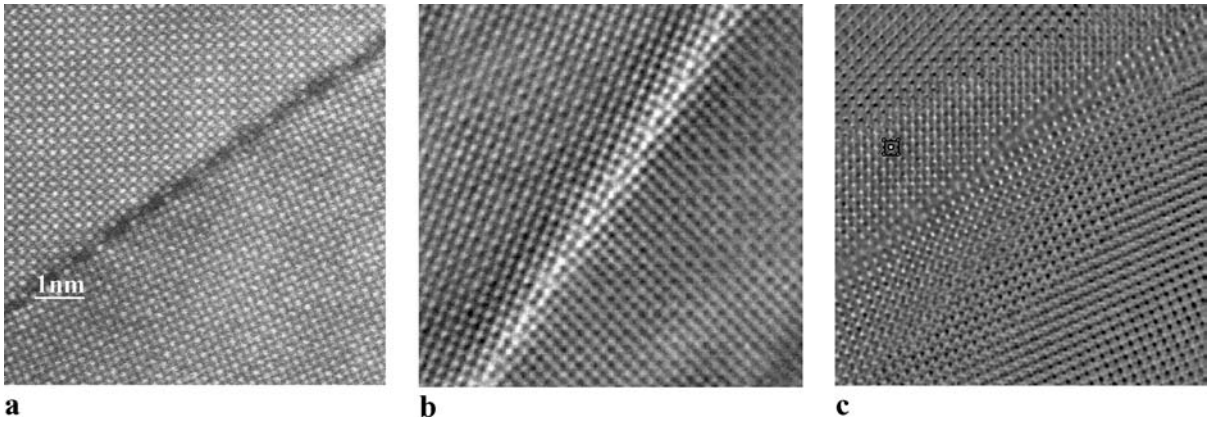

Figure 2 (a) HAADF image (Tecnai F20); (b) High voltage TEM lattice image (ARM); (c) Phase of the reconstructed electron exit wave (CM300). The scheme of SrTiO3 unit is superimposed in c ($a = 0.3905$ nm).

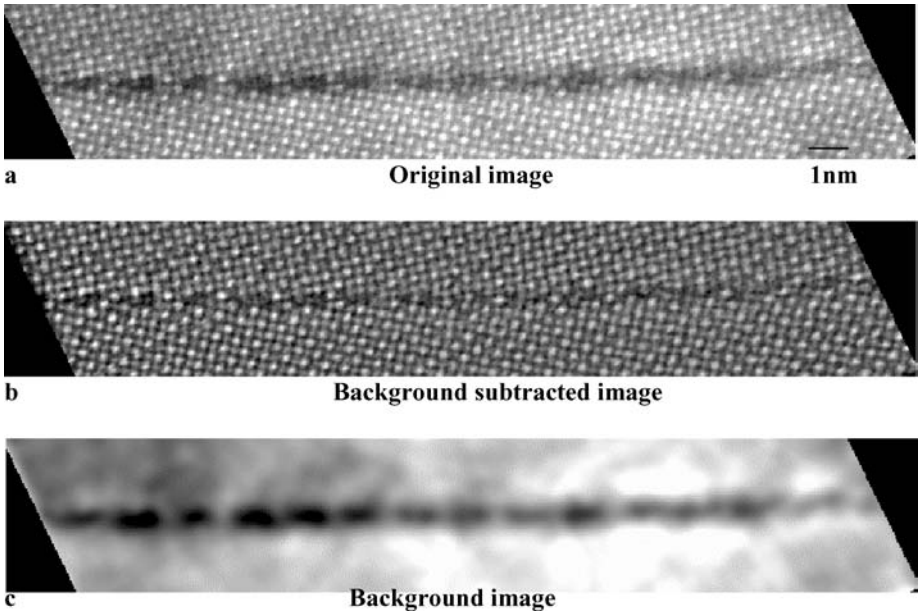

Figure 3 Experimental HAADF (a) original image; (b) background subtracted image; (c) background image.

A closer inspection of the signal (Fig. 3c) uncovers a quasi-periodic intensity fluctuation along the boundary. We argue that the GB is sensitive to the chemo-mechanical thinning process applied during the tripod preparation procedure. The classic solution for the final polishing is a base of $7 < \mathrm{pH} < 11$. Since this etch is not charge neutral, it is likely that a negatively charged GB will be subject to locally varying etch rates if the charges are distributed unevenly. Such doping related etch rates are common to solutions with $\mathrm{pH} > 7$ and were investigated in doped semiconductors [23]. The observed contrast change at STO GB's is found in most investigations. In fact, it seems that most sample preparation techniques cause boundaries grooving in STO. This effect is currently subject of ongoing research since it possibly provides a direct map of the charge distribution with nanometer resolution.

Since in projection a missing column atom cannot be distinguished from a surface step, there is a principal inability to discriminate between a local thickness change and the occupation of lattice sites with atoms that hampers a quantitative investigation of local stoichiometry. Therefore, the paper addresses mostly structural aspects even though we expect the formation of native point defects at the boundary and we will produce evidence for the presence of oxygen vacancies.

3. Results

3.1. HAADF Imaging

The Wiener filtered HAADF image of Fig. 4 visualizes a large section of the GB. The two distinctly different intensity maxima in the bulk of the material correspond to Sr ($Z = 38$) and TiO ($Z = 22$, $Z = 8$) columns in [001] projection. They can be discriminated because the contrast depends on the atomic number Z [24]. Oxygen columns are not visible. At the grain boundary, this chemical distinction becomes less evident since the sample is thinner. There, an identification of Sr and TiO atom columns can be supported assuming continuity of the surrounding matrix towards the GB.

The GB contains 14 structural units and 4 defects that are introduced by the deviation from the perfect coincidence orientation [25]. The origin of the structural units is chosen such that they correspond to boundary sites common to the two crystals. These lattice sites repeat with a periodicity of 1.4 nm. An identical periodicity is found in the background image of Fig. 3c and by comparison it is seen that preferential etching does not occur at the origin of the structural units but rather within the structural units themselves.

It is possible to discriminate 3 structurally different units that are shown in Fig. 5: one unit is delimited by TiO columns that are common to both crystals (TiO

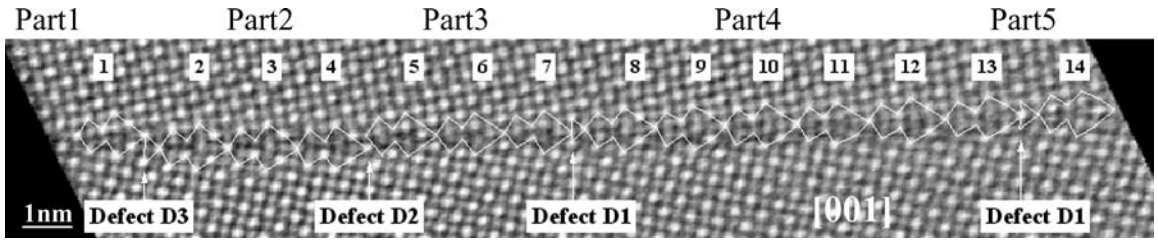

Figure 4 Wiener filtered image of the background subtracted HAADF image showing periodic arrangement series of different structural units separated by defects. The units 5 to 7 and 14 are centered on TiO columns at the GB. All the other units are centered on Sr columns. The units are drawn schematically by segments relating columns of same nature.

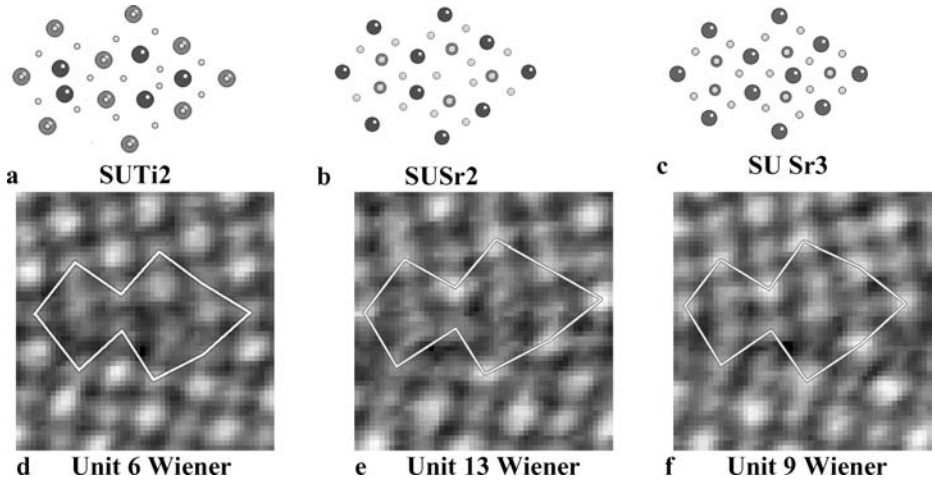

Figure 5 The SrTiO3 Σ13 grain boundary contains 3 distinctly different structural units $SUTi_2$ (a), $SUSr_2$ (b) and $SUSr_3$ (c). In (a) the unit cell is centered on TiO columns, in (b) and (c) on Sr columns. For a better visualization the background subtracted HAADF image of Fig. 3b was Wiener filtered. The length of the unit is 1.41 nm.

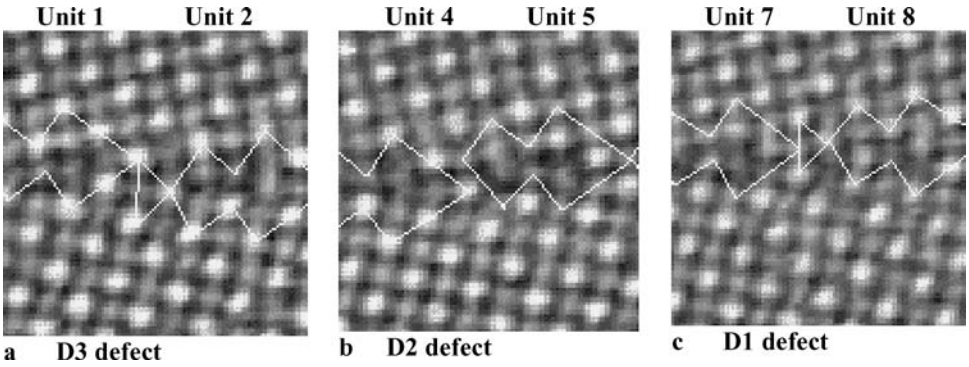

Figure 6 Enlargement of Fig. 4 showing the GB defects: (a) D3, (b) D2, (c) D1.

centered: $SUTi_2$ in Fig. 5a) and two units are delimited by Sr columns (Sr centered: SUSr, Fig. 5b and c). They differ by the addition of one Sr column in the center of the cell ($SUSr_3$). Neighboring atom columns of the same chemical composition appear at the GB, as reported before. We find 10 Sr centered GB units (number 1–4 and 8–13) and 4 Ti centered units (number 5–7 and 14) in the field of view. The oxygen atomic positions in the proposed models are suggested from the EWR results (see Section 3.2).

In Fig. 4, four defects separate five regions containing a periodic arrangement of similar structural units. Two of the defects are identical (defects D1 of same geometry but either centered on Sr or on TiO columns). The three different defects are shown in Fig. 6. Their Burgers vectors are determined by measuring the difference between two circuits relating two similar sites of the structural units before and after the considered defect [26]. Sr and TiO columns are not distinguished. If S1 is the circuit in the upper crystal 1 and S2 the circuit in the lower one then $\underline{b}$ is given by $\vec{b} = S1 - RS2$, where R is the rotation matrix between the two crystals.

The defect D1 is located between structural units 7 and 8 and units 13 and 14. Its Burgers vector is $\vec{b}_{D1} = \frac{1}{13}[320]$, perpendicular to the GB. It accounts for the deviation from the coincidence orientation and corresponds effectively to a unit S or S^* of the delimiting Σ 1*(110) GB. This partial dislocation is not a DSC dislocation according to [25] as it should relate two similar structural units with the same chemistry.

The defect 2 is seen between the structural units 4 and 5 of the HAADF image. Its Burgers vector is $\vec{b}_{D2} = \frac{1}{13}[\bar{2}30]$ in the upper crystal. It creates a 0.27 nm high step.

The defect D3 is located between structural units 1 and 2 and corresponds to a translation vector of the GB since the associated structural units are similar. Its Burgers vector is $\vec{b}_{D3} = \frac{1}{13}[510] = \vec{b}_{D1} - \vec{b}_{D2}$. The related step height is again 0.27 nm.

The number of structural units between the dislocations containing a $\vec{b}_{D1}$ component is 6, which one would expect from the tilt deviation of the coincidence orientation. Their periodic arrangement is highlighted in dark field imaging shown in Fig. 7.

HAADF imaging is characterized by a good discrimination between Sr and TiO columns and little sensitivity

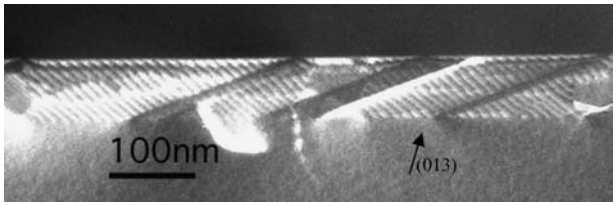

Figure 7 Dark field image of the grain boundary showing the intrinsic dislocation array and some extrinsic dislocations.

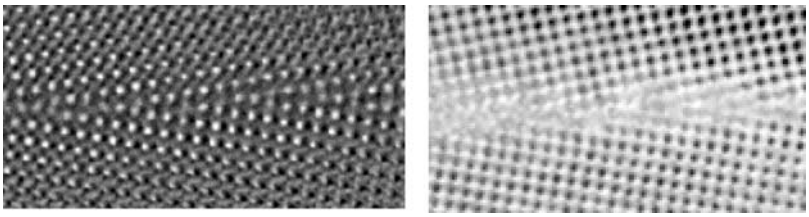

Figure 8 (a) Phase image from exit wave reconstruction; (b) amplitude image fit for 40 Å thickness.

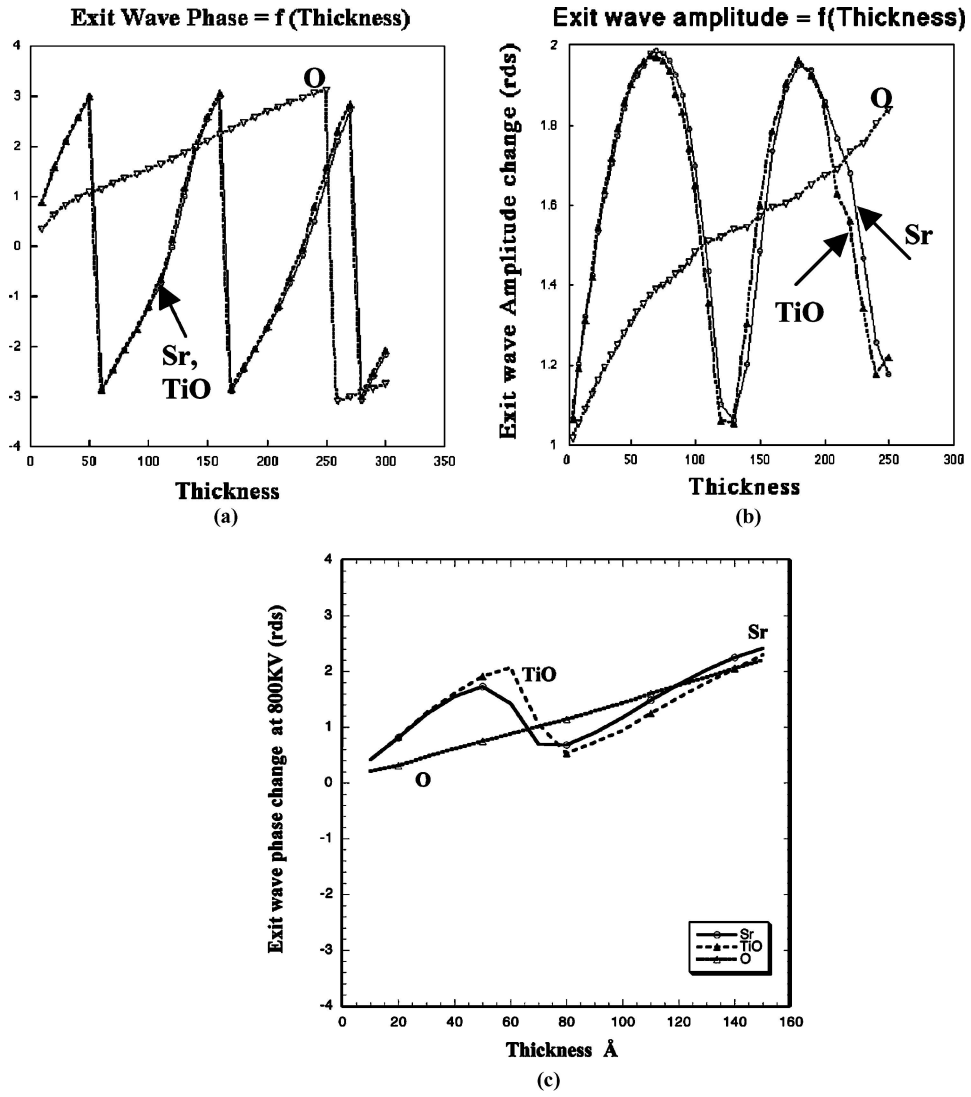

Figure 9 Exit wave phase (a) and amplitude (b) variations (CM300) as a function of the thickness. TiO and Sr show the same behavior; (c) Exit wave phase variation (ARM) at 800 kV. In the range of 4–10 nm one can distinguish Sr and TiO atomic columns. The thickness values are in Å on the graphs.

to intensity changes with thickness except for the thin crystal areas at the grooved boundary. Oxygen columns cannot be detected. Further, our attempts to measure local lattice displacements from the HAADF image were of insufficient accuracy because of the present noise levels. Displacements are addressed later by measurements from phase contrast images.

3.2. Exit wave reconstruction (EWR)

Amplitude and phase of the GB's electron exit wave are reconstructed from a focal series of 20 lattice images and shown in Fig. 8. Here the grooving at the grain boundary required a local signal optimization that was performed by an established procedure that maximizes the phase signal (or minimizes the amplitude signal) while propagating the exit wave in steps of 0.5 nm with the TrueImage software package [27, 28]. It is seen from Fig. 8 that a large pattern change reflects the steep thickness change at the boundary. Fig. 9a and b show calculations of amplitude and phase intensity maxima that mark Sr, TiO, and O columns. It is seen that Sr and TiO columns cannot be distinguished if recorded with a 300 kV microscope because of an accidental intensity degeneracy that, however, can be removed by utilization of other acceleration voltages as shown in Fig. 9c. This calculated result is verified in the experiment and explains why Sr and TiO columns cannot be

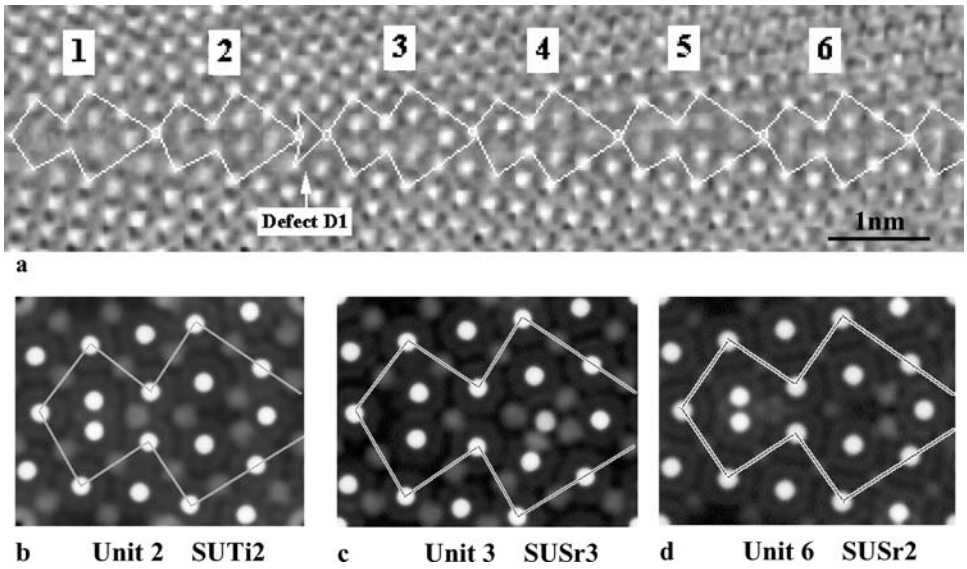

Figure 10 (a) Experimental exit wave phase image issued from the reconstruction with the scheme of the units. A dislocation defect D1 is located between unit 2 and unit 3; (b, c and d): simulation of the phase image of the structural units $SUTi_2$, $SUSr_3$ and $SUSr_2$ corresponding respectively to unit 1, 3 and 6.

distinguished in reconstructed exit waves but in lattice images recorded in a high voltage instrument.

The intensities oscillate with sample thickness and the oscillation period is 12 nm for the degenerated Sr/TiO columns but 52 nm for the O column. In thin crystals (<6 nm) they increase almost linear with sample thickness and intensity ratios can be used to determine the sample thickness if full occupancy is assumed. Alternatively, such graphs allow for a determination of the occupancy if the sample thickness is locally known.

The Fig. 10 shows the recorded boundary with superimposed structural units that reveal the presence of the defect D1. Clearly, it is not possible to extract from the image whether or not the individual units are Sr or TiO centered at the origin. If we assume a situation identical to the one shown in Fig. 6c, TiO centered structural units would extend to the left of the defect and Sr centered units are on its right side as shown in Fig. 10b through 10d. This choice is consistent with the arrangement of units in the HAADF image (Fig. 4). The EWR was optimized for each unit separately in order to account for a defocus change along the boundary. The phase image of unit $SUSr_3$ is depicted in Fig. 11.

In contrast to the HAADF image, the O columns are detectable in the reconstructed exit wave as shown in Fig. 11 that depicts unit 3 at a larger magnification with the crystal structure superimposed. The extra Sr column in the unit's center is directly visible and column splitting is noticeable with a projected distance of about 0.9 Å. Column splitting was predicted but not observed until now. Moreover, Fig. 11 is the highest resolution image of a non-periodic grain boundary site. This observation proves sub Ångstrom resolution. Multi-slice calculations confirm that the line trace of Fig. 11c can be simulated by half occupied Sr columns. A further examination of the O-, Sr-, and TiO columns is limited

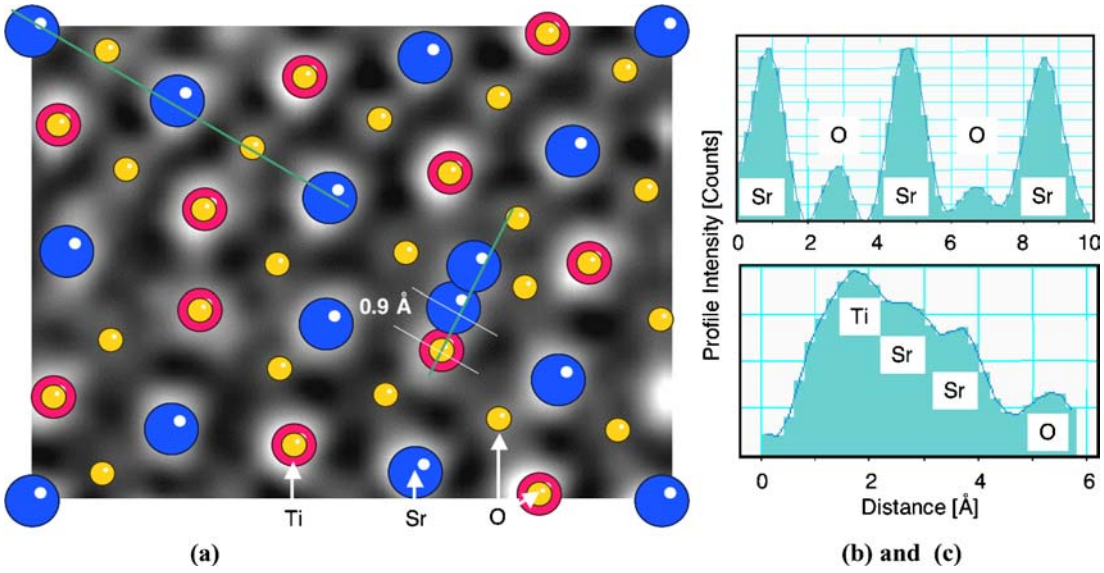

Figure 11 (a) Experimental exit wave phase image issue from the reconstruction for unit 3. The geometrical atomic model is superimposed. (b) Profile intensities along the [100] Sr-O profile line (top) and across the GB (bottom) as underlined on the line profiles of Fig. a.

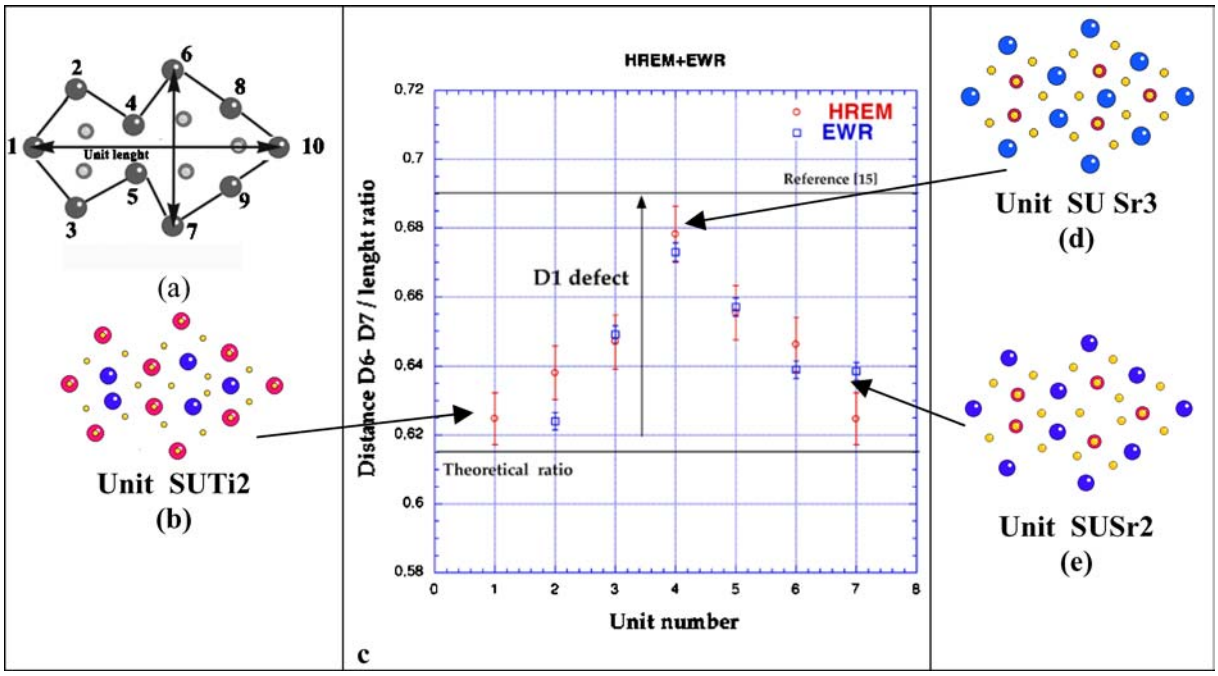

Figure 12 Graph showing the variation of the ratio D6–7/Unit length measured for each unit in the exit wave phase image. The values determined from the high voltage HRTEM image are also shown. In (a) the scheme of the unit showing a horizontal arrow for the unit length D1–10, and a vertical arrow for the D6–D7 distance.

because of the rapid thickness change at the boundary that makes a systematic discrimination between thickness and stoichiometry impossible. Only in specific cases such as shown in Fig. 11b one can assume constant local thickness since the intensity of three adjacent Sr columns is almost constant. In this case the recorded intensity variation of the two O columns must be attributed to a reduction of the O occupancy that can be estimated. Taking the larger Sr/O intensity as a measure of thickness, one estimates that the sample is 5 nm thick at this point by use of Fig. 9a. The oxygen occupancy is assumed to be 1. A 1/3 signal reduction of the adjacent O column would correspond to an oxygen occupancy of only 66%. Such measurements give estimates for possible O fluctuations within GB unit cells.

The presence of different structural units along the grain boundary suggests that the grain boundary expansion cannot be constant along its length. Measurements of the aspect ratio (width/length) of individual GB unit cells confirm this expectation and are shown in Fig. 12. It is seen that TiO and Sr centered units exhibit an almost identical expansion if the measurements are taken from unit cells that are separated by a few translation periods from the defect. Close to the defect we find that its presence alters the GB expansion normal to the GB from expected values of 0.108 nm to a maximum of 0.184 nm and it is reasonable to find a split Sr column in the center of GB units that are expanded most.

The reconstructed exit wave truly complements the HAADF image: Sr and TiO columns cannot be discriminated if images are recorded at 300 kV. However, oxygen columns are now visualized at the interface and in the bulk of the material. To our knowledge it is for the first time that oxygen columns are resolved at a GB in STO. A superior signal to noise ratio allows for displacement measurements with pm precision, which was not possible in the HAADF image because the grain boundary expansion did not exceed limits imposed by the noise.

3.3. High voltage lattice imaging

A magnified lattice image of the GB recorded with the ARM is shown in Fig. 13. Structural units as defined in HAADF image are again overlaid and they reveal the presence of the defect D1 in the field of view. A comparison between experimental—and simulated images reveals strong thickness and defocus variations both parallel and perpendicular to the GB. The thickness ranges from 70 Å at the GB to 120 Å at the edge of the image and the defocus from −660 to −580 Å. The weak sinusoidal pattern oscillation in the bulk of the material can be related to Sr and TiO columns by image simulations (Fig. 13c). The higher acceleration voltage is of advantage because it lifts the accidental intensity degeneration that is present in pictures recorded with 300 kV (Fig. 9c).

As a result, the assignment of TiO centered units to the left of the defect (1–3) and Sr centered units to its right (4–7) is unique. The 3 different GB units can be distinguished from simulated images (Fig. 14). However, the poorer signal to noise ratio of the experiment makes unit identification doubtful.

Measurements of the grain boundary expansion around defect D1 are depicted in Fig. 12. By comparison, it is clear that expansion values measured from the lattice image and the reconstructed exit wave agree well. Furthermore, the identical result justifies the TiO and Sr origin assignment that was assumed for the reconstructed exit wave. It is evident that a similar analysis of the HAADF image should also reproduce these findings. Indeed, we observe an equivalent tendency in the HAADF image that, however, suffers from a lack of attainable precision.

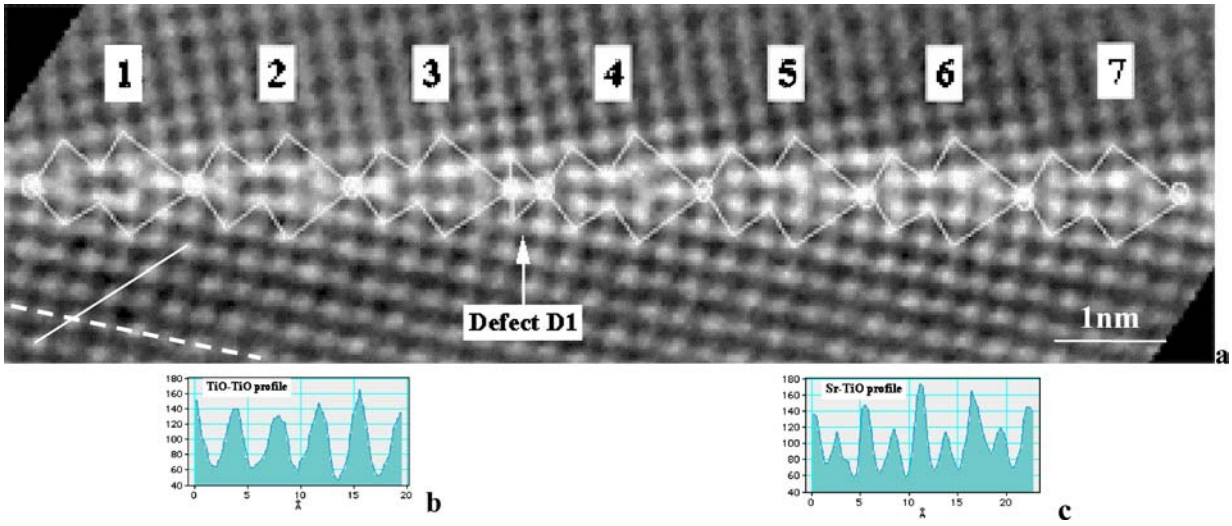

Figure 13 (a) Experimental HRTEM image showing the scheme of the Σ13 structural units. (b and c) Intensity profiles along [110] (dashed line in (a)) and [100] (full line in (a)). The highest peaks correspond to Ti-O columns.

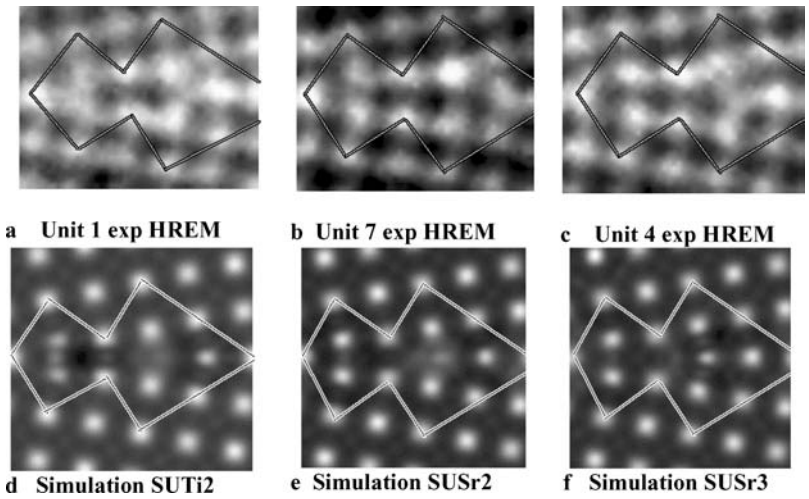

Figure 14 Experimental HRTEM images for unit 1 (a), unit 7 (b) and unit 4 (c) and simulated images for $SUTi_2$ (d), $SUSr_2$ (e) and $SUSr_3$ (f).

GB units 1 and 7 are separated most from the defect and exhibit a rather small GB expansion of 14%. In previous publications [7] larger GB expansion values of the order of the (320) interplanar spacing were reported. Since their aspect ratio is the same but their chemistry is different, a comparison of column positions inside the units is of interest. The distance D (A–B) between the closest similar atom columns depends on their chemical nature (Fig. 15): It is larger for TiO columns (2.30–2.36 Å) than for Sr columns (1.70–1.77 Å). Moreover, the ratio D (A − B)/(GB unit length) is almost constant with a value of 0.165 (Fig. 14) in Sr centered units and 0.125 in TiO centered units.

In summary, lattice imaging with a high voltage instrument yields similar results than extractable from the HAADF image. The chemical distinction is, however, poorer while column positions can be pinpointed with a better precision. In Table I we compare all three experiments.

4. Discussion

Novel structural units of the GB are defined by a coincidence lattice approach and the grain boundary is found to contain periodic arrangements of structural units separated by defects that can be described as grain boundary dislocations.

In this materials system HAADF imaging and HVTEM allow for a direct identification of Sr and TiO columns in [100] direction. A determination of column positions is feasible in case of lattice imaging by HVTEM but lacks of accuracy in case of HAADF imaging because the boundary expansion is too small (14%) to be measured at the given noise level. In both cases, oxygen columns cannot be detected.

Complementary, the reconstruction of the electron exit wave enables the identification of oxygen columns.

TABLE I Table showing the complementarities of the HAADF imaging and EWR techniques and the similarities between HREM and HAADF imaging techniques

Technique	Distinction of TiO and Sr columns	Detection of oxygen columns	Accuracy of displacement Measurements $\pm \Delta d$ (nm)
HREM@800 KV	Yes	No	0.006 nm
HAADF@200 KV	Yes	No	0.014 nm
EWR@300 KV	No	Yes	0.002 nm

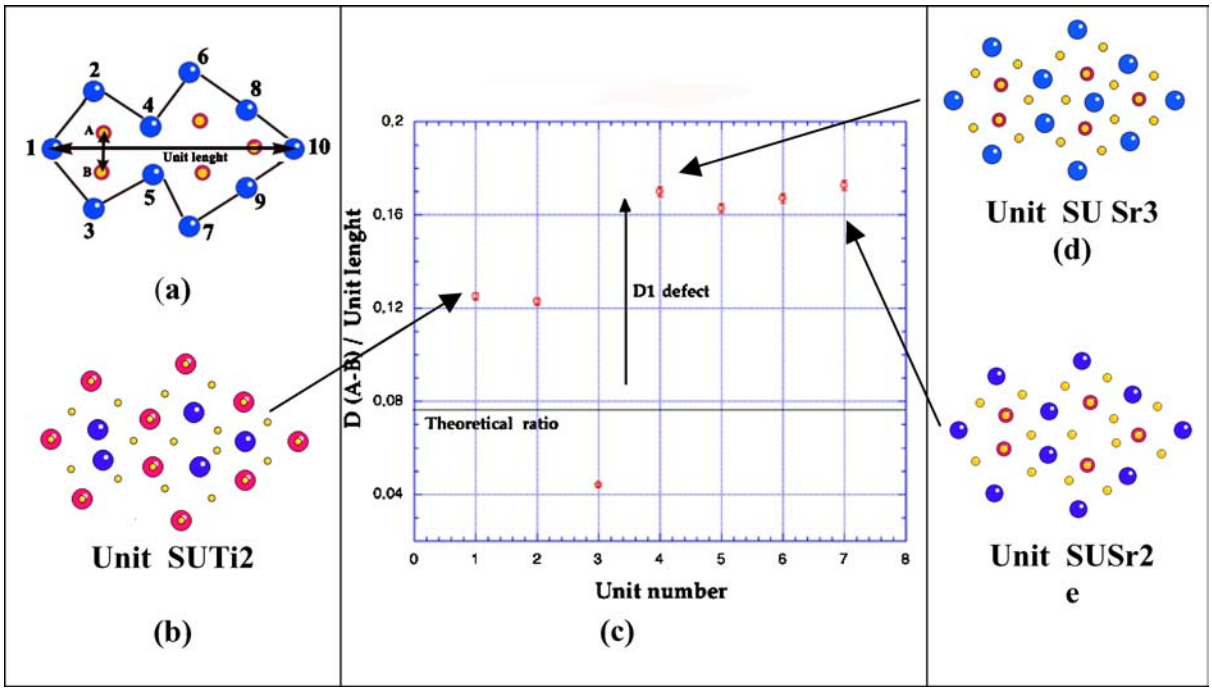

Figure 15 Graph showing the variation of the ratio of the D(A-B)/length for the different structural units in the HRTEM image.

A best signal to noise ratio allows determining column positions with pm precision. The measurements are not dominated by statistical—but by systematic errors of 1–2 pm that relate to residual lens aberrations. Moreover, a quantitative intensity interpretation is possible if the sample thickness is constant. In praxis, however, grain boundary grooving limits such interpretations to a few specific cases. In investigated single cases a reduction of the oxygen occupancy by 30–40% seems possible.

Improvements of sample preparation techniques seem generally necessary in order to get a better understanding of local stoichiometry.

The defined GB unit cells can be classified by three structural units called $SUSr_2$, $SUSr_3$, and $SUTi_2$ where Ti_2 describes a unit cell centered on TiO columns while $Sr_{2,3}$ unit cells are centered on Sr columns. Sr_3 contains an additional Sr column in comparison to Sr_2. The arrangement of oxygen columns is the same across all units. In each unit, closely spaced and chemically identical column pairs occur at the GB core. Four such pairs can be found in $SUSr_2$ and $SUTi_2$ while $SUSr_3$ only contains three pairs.

The GB expansion is small (14%) but increases towards defects. We conclude that the GB is compact and thereby unexpectedly different from models derived from previous HAADF investigations [7–9] or from calculations [10–13]. In these models, the GB structure is closer to a perfect crystal with respect to the atom arrangement and chemical bonding because only two Sr atom columns are in close proximity there. Moreover, we find bond length differences between the Sr-Sr and TiO-TiO column pairs.

If we ignore a possible partial column filling, as observed for a Sr column here and for TiO columns before [11, 14–16], the units would exhibit the following stoichiometric deviations: The $SUSr_3$ units would lack an oxygen column, the $SUSr_2$ and $SUTi_2$ units would be neutral but incorporate additional TiO_2 and SrO, respectively. The presence of a high number of similar columns in close proximity would lead to a highly charged GB, which can explain the large preferential etching at the center of the cells where the pairs reside.

In total we recorded twice as many $SUSr_3$ units than other units, which indicates that an additional Sr column in coincidence at the GB is of lower energy configuration than one would expect. Sr column splitting is found in cells close to defects where the aspect ratio of GB unit cells is the largest.

In terms of the SU/GBD approach, only the $SUSr_3$ unit can be created by combining the simpler S and S' units of the $\Sigma 1^*(110)$ GB with one B' unit of the Σ 5 (210) GB (Figs 1 and 16a) that corresponds to a dislocation core [16]. In contrast, one TiO column is missing in unit B' of [16], and the calculated structure of the (210) tilt GB centered on Sr columns contains only one TiO column instead of three columns in the B' unit [15]. Finally, one can recognize A and A' units of $36^\circ\sum 5(310)$ (Fig. 1) in the GB units (Fig. 16b). These units also appear in the 58° [001] tilt GB [11], although this $\Sigma 5(310)$ GB is not a delimiting GB for the $\Sigma 13$ (320) and the 58° [001] tilt GB's. Here, we have the same geometry whatever the unit of a lowest energy configuration may be. These results show

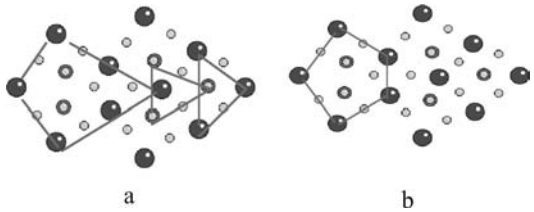

Figure 16 The $SUSr_3$ structural unit can be described as a combination of $\Sigma 5$ (B' in Fig. 1) and $\Sigma 1 *$ (S and S' in Fig. 1) structural units. The unit schemed in (b) corresponds to the favored $\Sigma 5(310)$ GB structural unitt A'

that our near [001] Σ13 tilt GB contains a multiplicity of GB unit structures. This finding questions the prediction that [001] tilt GBs can be formed by a limited number of structural units. Our boundary is probably of high-energy configuration. The presence of localized defects indicates a tendency to maintain a coincidence lattice.

5. Conclusion

We have shown that electron exit wave reconstruction complements HAADF imaging because of its unique ability to image oxygen columns. In addition, EWR allows for a determination of column position with pm precision and—principally—for a determination of stoichiometry by intensity quantification. Similar to HAADF images, Sr and TiO columns can be distinguished in high voltage lattice images where the high voltage lifts an accidental intensity degeneracy that is present if [100] images are recorded at 300 kV.

A preferential etching during sample preparation favors GB grooving and creates periodic holes that seem to map a charge distribution with a nanometer resolution. A further investigation of the local stoichoimetry will, however, be necessary since the grooving severely limits quantitative intensity interpretations. Estimates suggest an oxygen vacancy formation on 30–40% of the oxygen lattice sites at the boundary. Sub-Ångstrom resolution reveals a Sr column splitting for the first time.

We have identified 3 new structural units of the Σ13 GB, which are either centered on Sr columns or on TiO columns. This grain boundary is formed by a multiplicity of structural units, which contain three or four column pairs with identical elements in close proximity, probably a high energy configuration.

Acknowledgement

The project was sponsored by the Director, Office of Science, Office of Basic Energy Sciences, of the U.S. Department of Energy under Contract No. DE-AC03-76SF00098. This project was sponsored by the General Direction of the French Defense (DGA) under the contract N°. 01 60 061/DSP/SREA/SC/SR and N°.03 60 00 034/DSP/SREA/SC/SR.

References

1. A. F.DEGARDIN and A. KREISLER, in "Crystal Growth in Thin Solid Films: Control of Epitaxy" edited by M.Guilloux-Viry and A. Perrin (Publisher Research Signpost, 2002) Chapt. 1.
2. D. DIMOS, P. CHAUDHARI and J. MANNHART, *Phys. Rev.* **B 41** (1990) 4038.
3. C. C. TSUEI, J. R. KIRTLEY, C. C. CHI, L. S. YU-JAHNES, A. GUPTA, T. SHAW, J. Z. SUN and M. B. KETCHEN, *Phys. Rev. Lett.* **73** (1994) 593.
4. P. CHAUDHARI, J. MANNHART, D. DIMOS, C. C. TOURI, J. CHI, M. M. OPRYSKO and M. SCHEUERMANN, *ibid.* **60** (1988) 1653.
5. ZAOLI ZHANG, WILFRIED SIGLE, FRITZ PHILLIPP and MANFRED RUEHLE, *Science* **302** (2003) 846.
6. C. L. JIA and K. URBAN, *ibid.* **303** (2004) 2001.
7. N. D. BROWNING and S. J. PENNYCOOK, *J. Phys.* **D29** (1996) 1779.
8. N. D. BROWNING, S. J. PENNYCOOK, M. F. CHISHOLM, M. M. MCGIBBON and A.J. MCGIBBON, *Interf. Sci.* **2** (1995) 397.
9. M. M. MCGIBBON, N. D. BROWNING, A. J. MCGIBBON and S. J. PENNYCOOK, *Philosoph. Mag.* **A73** (1996) 625.
10. M. M. MCGIBBON, N. D. BROWNING, M. F. CHISHOLM, A. J. MCGIBBON, S. J. PENNYCOOK, V. RAVIKUMAR and V. P. DRAVID, *Science* **266** (1994) 102.
11. R. F. KLIE, M. BELEGGIA, Y. ZHU, J. P. BUBAN and N. D. BROWNING, *Phys. Rev. B* **68** (2003) 214101.
12. V. RAVIKUMAR, V. P. DRAVID and D. WOLF, *Interf. Sci.* **8** (2000) 157.
13. V. P. DRAVID and V. RAVIKUMAR, *ibid.* **8** (2000) 177.
14. H. CHANG, Y. CHOI J. D. LEE and H. YI, *Appl. Phys. Lett.* **81** (2002) 3564.
15. M. KIM, G. DUSCHER, N. D. BROWNING, KARL SOHLBERG, S. T. PANTELIDES and S. J. PENNYCOOK, *Phys. Rev. Lett.* **86** (2001) 4056.
16. G. DUSCHER, J. P. BUBAN, N. D. BROWNING, M. F. CHISHOLM and S. J. PENNYCOOK, *Interf.Sci.* **8** (2000) 199.
17. R. W. BALLUFFI and P. D. BRISTOWE, *Surf. Sci.* **144** (1984) 28.
18. A. SUTTON and R. W. BALLUFFI, in "Interfaces in Crystalline Materials", (Clarendon Press, Oxford, 1995)
19. J. P. MORNIROLI, "Diffraction Electronique en Faisceau Convergent a Grand Angle (LACBED)" edited by Societe Française des (Microscopies, 1998).
20. M. A. O'KEEFE, C. J. D. HETHERINGTON, Y. C. WANG, E. C. NELSON, J. H. TURNER, C. KISIELOWSKI, J.-O. MALM, R. MUELLER, J. RINGNALDA, M. PAM and A. THUST, *Ultramicroscopy* **89** (2001) 215.
21. C. KISIELOWSKI, C. J. D. HETHERINGTON, Y. C. WANG, R. KILAAS, M. A. O'KEEFE and A. THUST, *ibid.* **89** (2001) 243.
22. website http://www.totalresolution.com
23. K. E. PETERSON, *Proceedings IEEE* **70** (1982) 420.
24. D. E. JESSON and S. J. PENNYCOOK, *Proc. R. Soc. Lond.* **A449** (1995) 223.
25. W. BOLLMANN, in "Crystal defects and Crystalline Interfaces" (Heidelberg, Springer Verlag, 1970)
26. A. H. KING and D. A. SMITH, *Acta Cryst.* **A36** (1980) 335.
27. W. M. J. COENE, A. THUST, M. OP DE BEECK and D. VAN DYCK, *Ultramicroscopy* **64** (1996) 10.
28. A. THUST, W. M. J. COENE, M. OP DE BEECK and D. VAN DYCK, *ibid.* **64** (1996) 211.

Received 17 September 2004
and accepted 31 January 2005